*Article*

# Surface Modification of ZrO$_2$ Nanoparticles with TEOS to Prepare Transparent ZrO$_2$@SiO$_2$-PDMS Nanocomposite Films with Adjustable Refractive Indices

**Hanjun Cho [1,†], Deunchan Lee [1,†], Suyeon Hong [1], Heegyeong Kim [1], Kwanghyeon Jo [1], Changwook Kim [2,\*] and Ilsun Yoon [1,\*]**

[1]  Department of Chemistry, Chungnam National University, Daejeon 34134, Korea; jhjnamoo@naver.com (H.C.); hjdc1278@gmail.com (D.L.); rieh10@cnu.ac.kr (S.H.); hgk205@daum.net (H.K.); jokh7707@naver.com (K.J.)
[2]  School of Electric Engineering, Kookmin University, Seoul 02707, Korea
\*  Correspondence: ncwkim@kookmin.ac.kr (C.K.); ilsunyoon@cnu.ac.kr (I.Y.)
†  These authors contributed equally to this work.

**Abstract:** Here, highly transparent nanocomposite films with an adjustable refractive index were fabricated through stable dispersion of ZrO$_2$ ($n$ = 2.16) nanoparticles (NPs) subjected to surface modification with SiO$_2$ ($n$ = 1.46) in polydimethylsiloxane (PDMS) ($n$ = 1.42) using the Stöber method. ZrO$_2$ NPs (13.7 nm) were synthesized using conventional hydrothermal synthesis, and their surface modification with SiO$_2$ (ZrO$_2$@SiO$_2$ NPs) was controlled by varying the reaction time (3–54 h). The surface modification of the NPs was characterized using Fourier-transform infrared spectroscopy, dynamic light scattering, X-ray photoelectron spectroscopy, scanning electron microscopy, transmission electron microscopy, and ellipsometry. The surface modification was monitored, and the effective layer thickness of SiO$_2$ varied from 0.1 nm to 4.2 nm. The effective refractive index of the ZrO$_2$@SiO$_2$ NPs at $\lambda$ = 633 nm was gradually reduced from 2.16 to 1.63. The 100 nm nanocomposite film was prepared by spin-coating the dispersion of ZrO$_2$@SiO$_2$ NPs in PDMS on the coverslip. The nanocomposite film prepared using ZrO$_2$@SiO$_2$ NPs with a reaction time of 18 h (ZrO$_2$@SiO$_2$-18h-PDMS) exhibited excellent optical transparency (T$_{average}$ = 91.1%), close to the transparency of the coverslip (T$_{average}$ = 91.4%) in the visible range, and an adjustable refractive index ($n$ = 1.42–1.60) as the NP content in the film increased from 0 to 50.0 wt%.

**Keywords:** adjustable refractive index; nanocomposite; zirconia nanoparticle; sol–gel method; surface modification

## 1. Introduction

Polymers are widely used in our daily lives and in industry because of their easy processing, flexible functions, and diverse applications [1]. Several chemical synthesis methods use modified polymer materials for multiple functionalities while maintaining their basic properties [2]. However, the practical development of polymers has limitations, such as high cost and difficult production [3,4]. Incorporating inorganic nanoparticles (NPs) into polymer matrices allows the polymers to take on the various functions of the added NPs and enhances their mechanical, thermal, optical, and plasmonic properties. Owing to these advantages, nanocomposites have been developed in various research and industrial fields for practical use as high-performance functional materials [1,5–12].

A representative application of nanocomposites is as transparent high-refractive-index materials that can effectively manipulate light. Therefore, these materials can play an essential role in the development of compact lenses, optical fibers, and high-efficiency mobile displays by improving light refraction and extraction [10–12]. To realize a transparent nanocomposite with a high refractive index, the following criteria must be satisfied [1]. First, considering applications utilizing the visible region, NPs and polymers should not

absorb light in the visible region (400–800 nm). Second, NPs added to increase the refractive index of a nanocomposite should have a high refractive index. Refractive index matching between the NP and polymer must also be considered; therefore, selecting appropriate materials for the NP and polymer is essential [13]. Third, the size of NPs should be negligibly small compared to the wavelength of light to prevent an increase in haze due to light scattering and a reduction in light transmission [13,14]. The agglomerate formation in NPs can cause strong light scattering [14]. Several studies have reported methods for the strengthening of chemical affinity or for the conforming of stable chemical bonds between NPs and polymers to avoid agglomeration [15–29].

Due to their high refractive index and transparency in the visible region, $ZrO_2$ NPs have been used in the development of transparent nanocomposite films with high refractive indices [25–29]. Many studies investigating the surface modification of $ZrO_2$ with organic molecules or polymers in order to avoid $ZrO_2$ agglomeration and achieve stable dispersion in the polymer matrix have been published [21–29]. A typical example of such materials is a commercial product from Pixelligent Technologies LLC (Baltimore, MD, USA) that uses $ZrO_2$ NPs 5–20 nm in size functionalized with organic molecules. However, this product can be used with epoxy, acrylic resins, or specific polymers [30–32]. In addition to the surface modification of $ZrO_2$ with organic materials, Vossmeyer et al. and Xu et al. reported the surface modification of $ZrO_2$ with inorganic materials, such as $SiO_2$. However, they did not show the fabrication of transparent nanocomposite films [21,22]. To the best of our knowledge, there have been no reports on the fabrication of transparent nanocomposite film with adjustable refractive indices utilizing $ZrO_2$ NPs surface-modified with only a $SiO_2$ layer.

For uniform dispersion of $ZrO_2$ NPs in a non-polar polymer with high molecular weight, like polydimethylsiloxane (PDMS), modifying the polar surface of NPs with appropriate organic molecules or polymers containing significantly different polarities is difficult [29–33]. Therefore, research on chemical synthesis methods for surface modification of NPs that can be easily accessed at the lab scale is required. In this study, we prepared $ZrO_2$ NPs with a size of 13.7 nm through conventional hydrothermal synthesis [22]. As shown in Figure 1, surface modification of $ZrO_2$ NPs with $SiO_2$ ($ZrO_2$@$SiO_2$ NPs) was performed through hydrolysis and polymerization of tetraethyl orthosilicate (TEOS) using the Stöber method [22]. We demonstrate that a transparent, thin nanocomposite film with an adjustable refractive index can be fabricated by dispersing $ZrO_2$@$SiO_2$ NPs in PDMS. The surface modification was characterized by transmission electron microscopy (TEM) with energy-dispersive X-ray spectroscopy (EDX) and X-ray photoelectron spectroscopy (XPS). Fourier-transform infrared spectroscopy (FT-IR) and dynamic light scattering (DLS) confirmed the growth of the $SiO_2$ layer on $ZrO_2$ NPs, which was controlled by the reaction time of the reaction between the NPs and TEOS ($\leq$54 h). Based on the growth of the $SiO_2$ layer, the effective refractive index of the $ZrO_2$@$SiO_2$ NPs was determined from the aqueous NP solution by ellipsometry. The effective thickness of the $SiO_2$ layer (0–4.2 nm) formed on the surface of the $ZrO_2$ NPs was calculated using the effective refractive index [34]. After 18 h of reacting with TEOS, the $ZrO_2$@$SiO_2$ NPs had an appropriate thickness (1.3 nm) for the $SiO_2$ layer that allowed stable dispersal in the PDMS matrix with a high refractive index. Depending on the $ZrO_2$@$SiO_2$ NP content ($ZrO_2$@$SiO_2$-18h), the refractive index of the nanocomposite films was adjusted from 1.42 to 1.60 in the visible region. The nanocomposite film exhibited excellent optical transparency ($T_{average}$ = 91.1%), close to the transparency of the coverslip ($T_{average}$ = 91.4%).

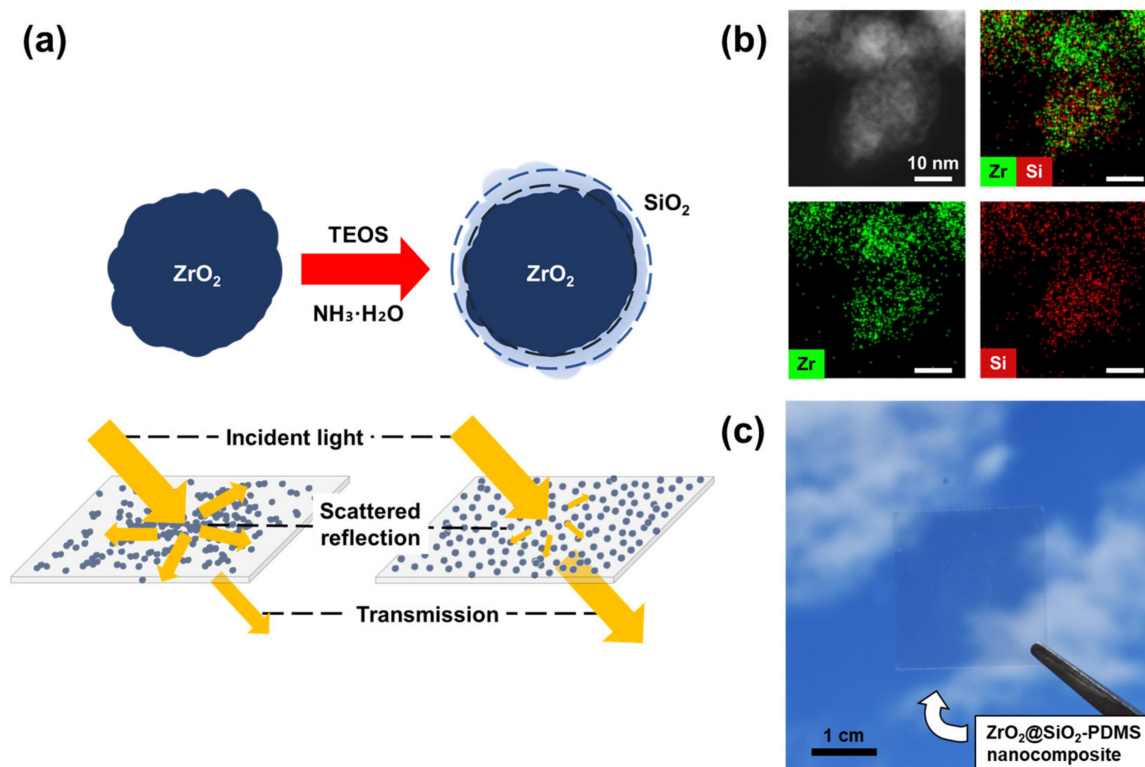**Figure 1.** (**a**) Schematic illustration of surface modification of $ZrO_2$ NPs using TEOS to prepare a transparent nanocomposite film with adjustable refractive index. (**b**) TEM-EDX images of $ZrO_2@SiO_2$ NPs indicating that the surface of $ZrO_2$ NPs was modified with the $SiO_2$ layer. (**c**) Photo of $ZrO_2@SiO_2$-PDMS nanocomposite film (100 nm thickness) containing 50 wt% $ZrO_2@SiO_2$ NPs.

## 2. Materials and Methods

### 2.1. Materials

Zirconyl chloride octahydrate ($ZrOCl_2 \cdot 8H_2O$, 98%), urea ($CH_4N_2O$, 99.0–100.5%), citric acid ($C_6H_8O_7$, ≥99.5%), TEOS ($Si(OC_2H_5)_4$, 98%), and aqueous ammonia (28 wt%) were purchased from Sigma Aldrich Co. (St. Louis, MI, USA). Ethanol, methanol, 2-propanol, and n-hexane were purchased from Samchun Chemicals Co. (Seoul, Korea). Commercial deionized water (18.25 MΩ, 25 °C) was purchased from Joylife Co. (Gimhae, Korea). A curing agent and PDMS base resin (Sylgard 184) were purchased from Dow Corning Co. (Midland, TX, USA). All the chemicals were used without further purification.

### 2.2. Synthesis of ZrO2 NPs

$ZrO_2$ NPs were synthesized through conventional hydrothermal synthesis, and the experimental details were modified for our environment [22]. A total of 0.8 g of zirconyl chloride octahydrate, 1.2 g of urea, and 0.4 g of citric acid were added to 25 g of deionized water. The solution was vigorously mixed for 30 min and then transferred to a precleaned Teflon hydrothermal reactor. The reactor was placed into a hydrothermal furnace and heated to 150 °C for 2 h. The reaction proceeded for 12 h, and then the hydrothermal reactor was cooled to room temperature. After cooling, the solution was centrifuged using methanol. Methanol was used for the primary centrifuge because it has greater solubility in urea than ethanol [35]. An additional centrifugation was performed with ethanol. The NPs were dried in a vacuum desiccator and used for TEOS surface modification.

### 2.3. Surface Modification of ZrO2 NPs with SiO2

Surface modification of $ZrO_2$ NPs was performed using the Stöber method, and the experimental details were modified for our environment [22]. A total of 46 mg of $ZrO_2$ NPs was dispersed in 1 g of deionized water. The $ZrO_2$ NP dispersion and 0.5 mL of aqueous

ammonia were added to 20 mL of 2-propanol. The solution was stirred at 1000 rpm at 30 °C, and then 24 μL of TEOS was added to the solution. To control the thickness of the $SiO_2$ layer, the reactions were performed at different reaction times of 3, 9, 18, 27, and 54 h. The solution was then centrifuged using 2-propanol, and additional centrifuges were performed with ethanol. The synthesized $ZrO_2@SiO_2$ NPs were then dried in a vacuum desiccator.

### 2.4. Preparation of ZrO_2@SiO_2-PDMS Nanocomposites

An equal amount of PDMS mixture and $ZrO_2@SiO_2$ NPs were added to hexane in a mass ratio of 1:1:100 (PDMS mixture:$ZrO_2@SiO_2$ NPs:hexane). The PDMS mixture was prepared by mixing the PDMS base with a curing agent at a weight ratio of 10:1 (PDMS base:curing agent). This mixture was fully dispersed by ultrasonication and dropped on the precleaned substrates (silicon wafer, coverslip). Spin-coating was performed at 1500 rpm for 30 s to produce the 100 nm nanocomposite film. Finally, the $ZrO_2@SiO_2$-PDMS nanocomposite film was cured in a convection oven for 5 h at 80 °C.

### 2.5. Characterizations

The morphologies of the $ZrO_2$ and $ZrO_2@SiO_2$ NPs were investigated with TEM (JEOL, JEM-ARM200F, Tokyo, Japan). For qualitative elemental analysis, EDX (Bruker, Quantax 400, Billerica, MA, USA) was performed using TEM. X-ray diffraction (XRD; Bruker, D8 Advance, Billerica, MA, USA) was used to determine the crystal structure of the $ZrO_2$ NPs. For the scanning electron microscopy (SEM, Tescan, Clara, Brno, Czech Republic) analysis, the $ZrO_2$ and $ZrO_2@SiO_2$ NPs were diluted to 1 g/L in ethanol and drop-casted on silicon wafers. Nanocomposite films were prepared on silicon wafers. The NPs and nanocomposite films were sputtered with Pt prior to SEM analysis. The elemental analysis of $ZrO_2$ and $ZrO_2@SiO_2$ NPs was verified using XPS (Thermo Scientific, K-alpha+, Waltham, MA, USA). FT-IR (Shimadzu, IRSpirit, Kyoto, Japan) at the CNU Chemistry Core Facility (Daejeon, Korea) was used to analyze the chemical bonds of the $ZrO_2$ and $ZrO_2@SiO_2$ NPs. NPs were diluted to 1 g/L in deionized water and ultrasonicated, and their hydrodynamic diameter was measured using DLS (Malvern Instruments, Zetasizer Nano ZS, Malvern, UK). An ultraviolet-visible spectrophotometer (UV-vis; Agilent Technologies, Agilent 8453, Santa Clara, CA, USA) at the CNU Chemistry Core Facility (Daejeon, Korea) was used to determine the optical characteristics of the aqueous solutions of the $ZrO_2$ and $ZrO_2@SiO_2$ NPs. The refractive indices of the NPs and nanocomposite films were measured using an ellipsometer (J.A. Woollam Co., RC-2, Lincoln, NE, USA). NPs were dispersed in deionized water to avoid light scattering and nanocomposite films were prepared on silicon wafers [36]. A lab-built UV-vis spectrophotometer with an integrating sphere was used for the optical characterization of nanocomposite films, and their reflectance and transmittance were measured on a coverslip. The extinction spectrum was obtained from the following relationship:

$$E(\lambda) + T(\lambda) + R(\lambda) = 100 \ (\%), \tag{1}$$

where $E(\lambda)$, $T(\lambda)$, and $R(\lambda)$ are the extinction, transmittance, and reflectance, respectively, at a given wavelength.

## 3. Results and Discussion

### 3.1. Material Characterization of ZrO_2 and ZrO_2@SiO_2 NPs

The crystal structure of synthesized $ZrO_2$ NPs was identified as the tetragonal phase, as shown in Figure S1, with XRD analysis [37,38]. The morphologies of the $ZrO_2$ and $ZrO_2@SiO_2$ NPs were investigated using SEM and TEM. As shown by SEM images (Figure 2a,d), the shapes of the $ZrO_2$ NPs were relatively irregular compared to those of the $ZrO_2@SiO_2$ NPs. NPs were agglomerated and it was difficult to find individual units of NPs. In contrast, individual units of $ZrO_2@SiO_2$ NPs were easily found in the SEM image. From the TEM analysis, the diameters of $ZrO_2$ and $ZrO_2@SiO_2$ NPs were measured to be 13.7 ± 3.1 nm (Figure 2b) and 16.3 ± 3.4 nm (Figure 2e), respectively. The $SiO_2$ layer was approximately

calculated from the radius difference of the $ZrO_2$ NPs and $ZrO_2@SiO_2$ NPs as $1.3 \pm 2.3$ nm. In addition, TEM and EDX analysis showed that Zr and Si coexisted in $ZrO_2@SiO_2$ NPs (Figure 1b), indicating that the surface of $ZrO_2$ NPs was modified with an nm-thick $SiO_2$ layer with the Stöber method.



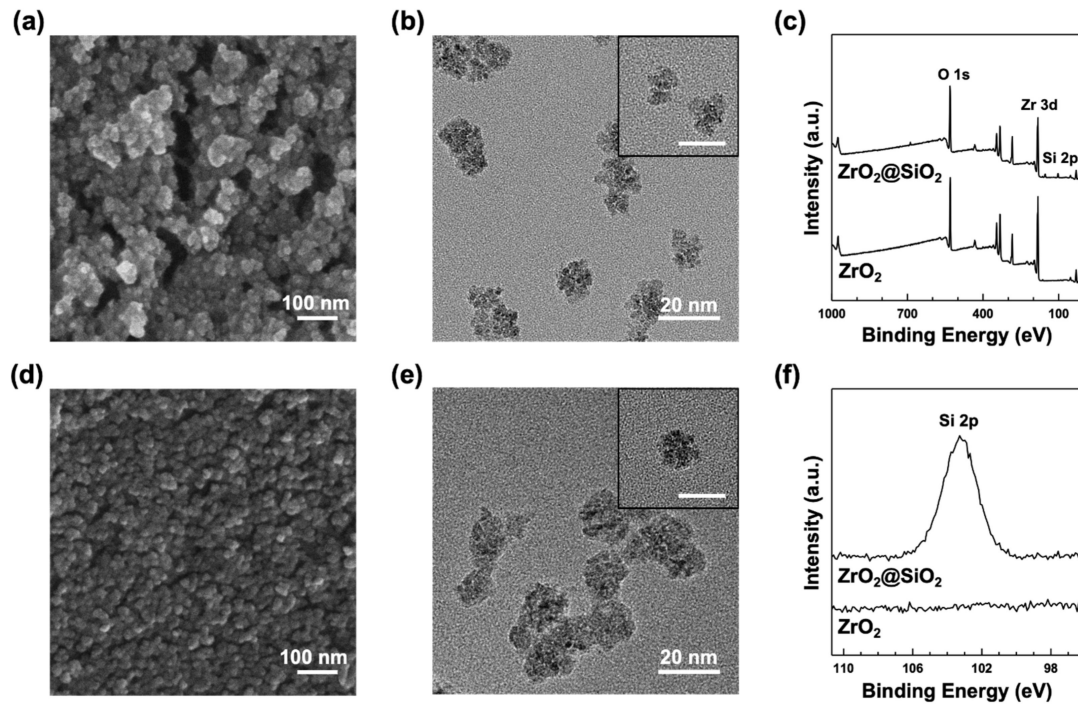**Figure 2.** (**a**) SEM and (**b**) TEM images of synthesized $ZrO_2$ NPs. The inset shows a representative TEM image of an individual $ZrO_2$ NP with a 20 nm scale. (**d**) SEM and (**e**) TEM images of $ZrO_2@SiO_2$ NPs. The inset shows a representative TEM image of an individual $ZrO_2@SiO_2$ NP with a 20 nm scale. (**c**) Low-resolution XPS spectra of $ZrO_2$ and $ZrO_2@SiO_2$ NPs. (**f**) High-resolution XPS spectra of Si 2p for both $ZrO_2$ and $ZrO_2@SiO_2$ NPs.

The elemental analysis of $ZrO_2$ and $ZrO_2@SiO_2$ NPs was performed using XPS. The corresponding low- and high-resolution XPS spectra are shown in Figure 2c,f, respectively. $ZrO_2@SiO_2$ NPs exhibited peaks of Zr (10.2%), Si (5.5%), O (47.7%), and C (36.6%), with a Zr:Si atomic ratio of 1.9. $Zr3d_{5/2}$ peaks in both NPs were detected at 182.6 and 182.7 eV, respectively, which were assigned to the binding energy of $Zr^{4+}$. The peaks of O1s were detected at 530.6 and 531.9 eV, respectively, which were assigned to the binding energy of Zr–O [39]. No significant signal of Si2p was observed in the $ZrO_2$ NPs; however, the $ZrO_2@SiO_2$ NPs showed the peak of Si2p at 103.3 eV, which was assigned to the binding energy of Si–O [39].

*3.2. The Surface Modification of $ZrO_2$ NPs with the $SiO_2$ Layer Controlled by the Reaction Time*

As described above, the surface modification of $ZrO_2$ NPs with the $SiO_2$ layer was controlled by varying the reaction time of the Stöber method [22]. FT-IR and DLS measurements were conducted to monitor the increase in the size of the $ZrO_2@SiO_2$ NPs as a result of the surface modification of the $ZrO_2$ NPs with the $SiO_2$ layer with the reaction time. The FT-IR spectra of the $ZrO_2@SiO_2$ NPs at different reaction times are shown in Figure 3a. Peak intensities observed at 1600 $cm^{-1}$ and 1100 $cm^{-1}$ can be attributed to the C=O stretching from residual citric acid on the $ZrO_2$ NP surface and the Si–O–Si asymmetric stretching from $SiO_2$, respectively [40,41]. As the reaction time increased, the absorption in the 1600 $cm^{-1}$ region decreased, while the absorption in the 1100 $cm^{-1}$ region increased, supporting the hypothesis that the growth of the $SiO_2$ layer can be controlled by the reaction time (Figure 3b). DLS spectra of $ZrO_2@SiO_2$ NPs show that the hydrodynamic

size of the ZrO$_2$@SiO$_2$ NPs gradually increased with the reaction time up to 27 h, as shown in Figure 3c,d. The hydrodynamic sizes of the ZrO$_2$ NPs and ZrO$_2$@SiO$_2$ NPs were larger than the physical sizes of the NPs determined from TEM analysis (Figure 2b,e). This was because the hydrodynamic size included not only the physical size of the NPs but also the thickness of the double layer, composed of the stern layer and the diffusion layer, on the NPs [42]. The hydrodynamic size was used limitedly to describe the NP size and DLS analysis showed that the surface modification of ZrO$_2$ NPs with a SiO$_2$ layer could be reproducibly controlled using the reaction time [42].
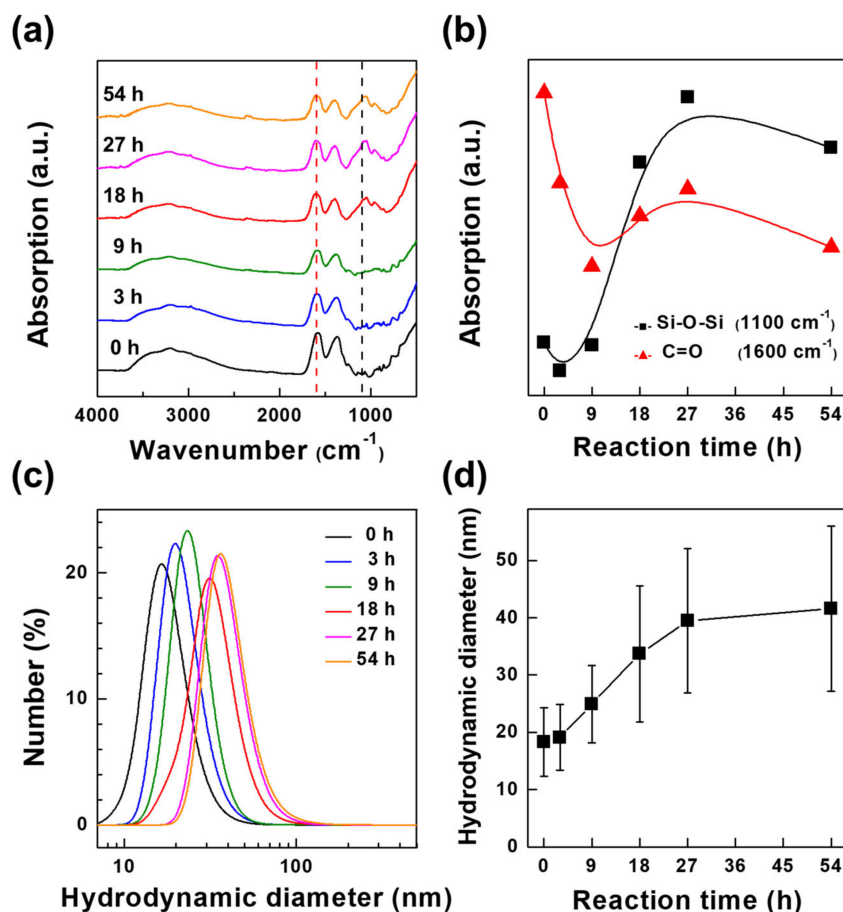


**Figure 3.** (**a**) FT-IR spectra of ZrO$_2$@SiO$_2$ NPs with different reaction times. Dashed lines indicate the peak positions corresponding to (black) Si–O–Si and (red) C=O bonds, respectively. (**b**) Changes in absorption intensities of ZrO$_2$@SiO$_2$ NPs according to the reaction time for (black) Si–O–Si and (red) C=O bonds. (**c**) Size distribution (hydrodynamic diameter) of ZrO$_2$@SiO$_2$ NPs with different reaction times, measured by DLS analysis. (**d**) Changes in mean hydrodynamic diameter of ZrO$_2$@SiO$_2$ NPs according to the reaction time. The error bar represents the standard deviation in the hydrodynamic diameters of the NPs.

### 3.3. Optical Characterization of ZrO$_2$ and ZrO$_2$@SiO$_2$ NPs

The effects of the surface modification of ZrO$_2$ NPs with different reaction times on optical properties, including the transmittance and effective refractive index, were evaluated using UV-vis spectroscopy and ellipsometry (Figure 4). UV-vis spectra of aqueous solutions of ZrO$_2$ and ZrO$_2$@SiO$_2$-18h NPs were obtained in the wavelength range from 250 to 900 nm (Figure 4a). The spectral features of the ZrO$_2$ and ZrO$_2$@SiO$_2$ NP aqueous solutions were almost identical; hence, light absorption by the SiO$_2$ layer was negligible. In both spectra, light absorption increased rapidly at below 300 nm, and the bandgap energy of 4.3 eV (288 nm) was determined from the Tauc plot (Figure 4a (inset)) [43]. Thus, the light absorption of NPs can be ignored in the visible range [44].
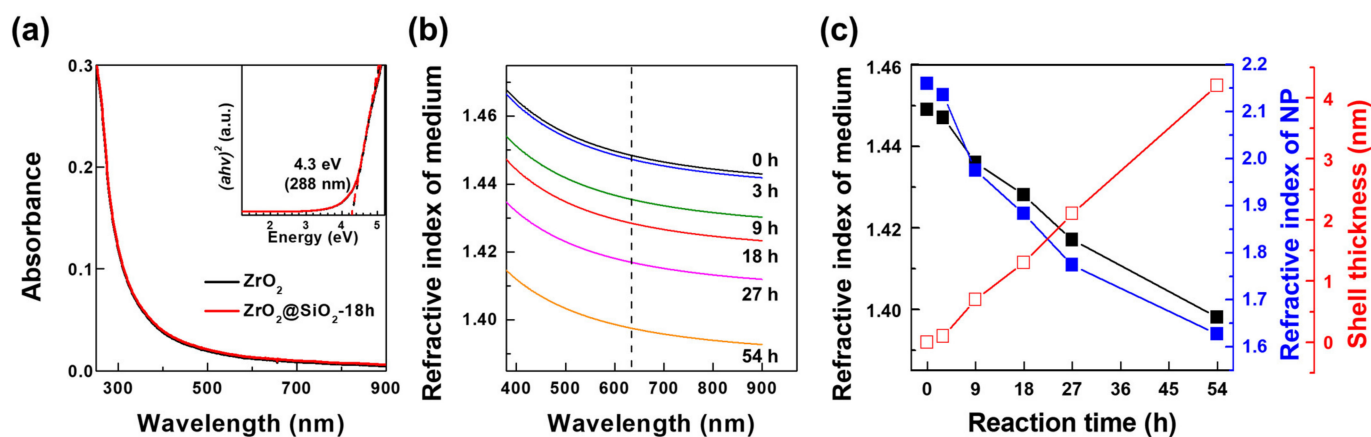
**Figure 4.** (**a**) UV-vis absorption spectra of (black) ZrO$_2$ and (red) ZrO$_2$@SiO$_2$-18h NPs. The inset shows the corresponding Tauc plots for (black) ZrO$_2$ and (red) ZrO$_2$@SiO$_2$-18h NPs. (**b**) Refractive index dispersions of aqueous solutions of ZrO$_2$@SiO$_2$ NPs prepared with different reaction times. All solutions were prepared with 50 wt% NP content. (**c**) Refractive (black) indices (at $\lambda$ = 633 nm) for ZrO$_2$@SiO$_2$ NP solutions with different reaction times and (red) calculated SiO$_2$ layer thicknesses, as well the (blue) effective refractive indices of ZrO$_2$@SiO$_2$ NPs.

To determine the refractive index dispersions of the NP aqueous solutions, psi and delta values were measured with the ellipsometer and fitted using the Cauchy model. The Cauchy model is appropriate for describing the refractive index dispersion in the wavelength region where the light absorption is negligible, as shown in the following equation:

$$n(\lambda) = A + \frac{B}{\lambda^2} + \frac{C}{\lambda^4}, \tag{2}$$

where A, B, and C are constants; $\lambda$ is the wavelength; and $n(\lambda)$ is the refractive index at a given wavelength [45]. The refractive index dispersions of the 50 wt% ZrO$_2$@SiO$_2$ NP aqueous solutions for each reaction time are shown in the wavelength range from 380 to 900 nm in Figure 4b. The refractive indices of each NP solution after 0, 3, 9, 18, 27, and 54 h were determined as 1.45, 1.45, 1.44, 1.43, 1.42, and 1.40 at $\lambda$ = 633 nm, respectively (the black line in Figure 4c, Table 1) [34]. Among the various effective refractive index approximations, the effective medium approximation (Equation (3)) gave calculated values for the effective refractive indices of the NP solutions closest to the experimental values measured in the ellipsometry analysis (Figure S2) [34,46–52]. The effective medium approximation (Equation (3)) was used as a simple model to calculate the effective refractive indices of ZrO$_2$@SiO$_2$ NPs for each reaction time (the blue line in Figure 4c), considering the refractive index of bare ZrO$_2$ NPs and a matrix (water) and the volume fraction of NPs in the solution (Figure S2, Table S1) [34,46–49]:

$$n_{eff}(\lambda) = \varphi n_{NP}(\lambda) + (1 - \varphi)n_{matrix}(\lambda), \tag{3}$$

where $n_{NP}(\lambda)$, $n_{matrix}(\lambda)$, and $n_{eff}(\lambda)$ are the refractive indices of the NPs, matrix, and NP solution, respectively, at a given wavelength. $\varphi$ is the volume fraction of NPs in the NP solution. $\varphi$ values were calculated as 0.141, 0.144, 0.161, 0.175, 0.192, and 0.244 for reaction times of 0, 3, 9, 18, 27, and 54 h, respectively. The refractive indices of each of ZrO$_2$@SiO$_2$ NP solution for the reaction times of 0, 3, 9, 18, 27, and 54 h were calculated as 2.16, 2.14, 1.98, 1.88, 1.77, and 1.63, respectively [34]. The refractive indices of the ZrO$_2$@SiO$_2$ NPs decreased with the reaction time and the surface modification of the ZrO$_2$ NPs. This was because the volume fraction of the high-refractive-index ZrO$_2$ ($n$ = 2.16) decreased relatively and that of the low-refractive-index SiO$_2$ ($n$ = 1.46) increased with the increasing reaction time during the surface modification of NPs, considering the same NP weight content in aqueous solutions. The shell thicknesses of the SiO$_2$ layers of the ZrO$_2$@SiO$_2$ NPs for

each reaction time of 0, 3, 9, 18, 27, and 54 h were calculated as 0.0, 0.1, 0.7, 1.3, 2.1, and 4.2 nm, respectively (the red line in Figure 4c) [34,46–49]. In particular, the calculated shell thickness of the $ZrO_2$@$SiO_2$ NPs for the reaction time of 18 h ($ZrO_2$@$SiO_2$-18h) was consistent with that given by the TEM analysis, as described above (Figure 2b,e).

**Table 1.** Refractive indices measured from $ZrO_2$@$SiO_2$ NP solutions with different reaction times and effective refractive indices, densities, and $SiO_2$ layer thicknesses calculated for $ZrO_2$@$SiO_2$ NPs. All refractive indices are represented at the wavelength of $\lambda$ = 633 nm (see Supplementary Materials for details).

| Reaction Time (h) | $ZrO_2$@$SiO_2$ NP Solution | $ZrO_2$@$SiO_2$ NP | | |
|---|---|---|---|---|
| | Refractive Index | Refractive Index [a] | Density [a] (g/mL) | $SiO_2$ Layer Thickness [a] (nm) |
| 0 | 1.45 | 2.16 | 6.10 | 0.0 |
| 3 | 1.45 | 2.14 | 5.98 | 0.1 |
| 9 | 1.44 | 1.98 | 5.19 | 0.7 |
| 18 | 1.43 | 1.88 | 4.74 | 1.3 |
| 27 | 1.42 | 1.77 | 4.20 | 2.1 |
| 54 | 1.40 | 1.63 | 3.47 | 4.2 |

[a] Values were calculated using the diameter of $ZrO_2$ NPs as determined by the TEM analysis (Figure 2) and the parameters given in Table S1.

### 3.4. Dispersibility of $ZrO_2$@$SiO_2$ NPs in PDMS

Since PDMS is a hydrophobic polymer matrix with a high molecular weight, surface modification is required for $ZrO_2$ NPs, which have $COO^-$ groups on the surface, to prevent the agglomeration of NPs in the PDMS matrix. $ZrO_2$@$SiO_2$ NPs can form chemical affinity with PDMS through the formation of bonds between the surficial Si–OH groups of NPs and PDMS chains [53–55]. Dispersion of $ZrO_2$@$SiO_2$ NPs in the PDMS matrix can be improved as the surfaces of the NPs are subjected to greater modification by the $SiO_2$ layer. However, to maintain a high refractive index, the $SiO_2$ layer for the $ZrO_2$@$SiO_2$ NPs should preferably be thin; therefore, determining the appropriate thickness of the $SiO_2$ layer is essential to achieve both transparency and a high refractive index in the nanocomposite film.

$ZrO_2$@$SiO_2$-PDMS nanocomposite films were prepared by dispersing $ZrO_2$@$SiO_2$ NPs subjected to different reaction times in the PDMS matrix and curing the mixture on a glass coverslip, as described above. SEM images and digital photographs were compared for the nanocomposite films to identify the dispersion of $ZrO_2$@$SiO_2$ NPs according to the surface modification (Figure 5). Figure 5a,b show top-view and (inset) 70 degree SEM images of 50 wt% $ZrO_2$-PDMS and $ZrO_2$@$SiO_2$-18h-PDMS, respectively. It was found that the surface modification of NPs using $SiO_2$ inhibited the agglomeration of the $ZrO_2$ NPs in PDMS and induced a uniform dispersion. In the case of $ZrO_2$@$SiO_2$-18h-PDMS, $ZrO_2$@$SiO_2$-18h NPs were dispersed without any recognizable agglomeration. However, in the case of $ZrO_2$-PDMS, $ZrO_2$ NPs were heavily agglomerated into several hundred nanometers. The change in transparency of the nanocomposite films according to the surface modification of the $ZrO_2$ NPs is shown in digital photographs in Figure 5c–e. $ZrO_2$-PDMS appeared opaque due to light scattering from the agglomeration of NPs (Figure 5d). $ZrO_2$@$SiO_2$-3h-PDMS also appeared opaque, indicating that the surface modification of the NPs was insufficient to achieve good dispersion in PDMS (Figure 5e). On the other hand, $ZrO_2$@$SiO_2$-18h-PDMS was transparent, to a similar degree as the PDMS, showing that NPs were well-dispersed in the matrix (Figure 5c,f); that is, unlike the $ZrO_2$ and $ZrO_2$@$SiO_2$-3h NPs, the $ZrO_2$@$SiO_2$-18h NPs had a sufficiently thick $SiO_2$ layer, leading to homogenous dispersion in PDMS.
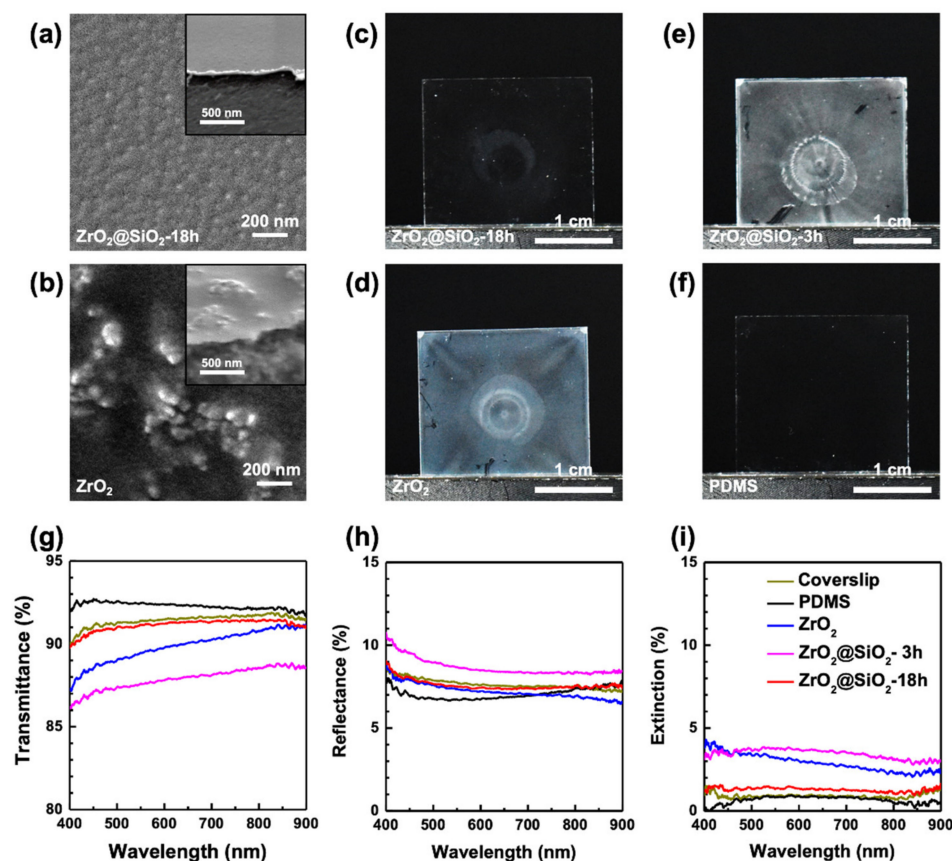
**Figure 5.** SEM images of (**a**) $ZrO_2@SiO_2$-18h-PDMS and (**b**) $ZrO_2$-PDMS films. The inset shows 70 degree SEM images of the film edges of (**a**) $ZrO_2@SiO_2$-18h-PDMS and (**b**) $ZrO_2$-PDMS films. Digital photos of (**c**) $ZrO_2@SiO_2$-18h-PDMS, (**d**) $ZrO_2$-PDMS, (**e**) $ZrO_2@SiO_2$-3h-PDMS, and (**f**) PDMS films. All films were prepared with 100 nm thickness on Si substrates or coverslips with NP contents of 50 wt%. (**g**) Transmittance (T), (**h**) reflectance (R), and (**i**) extinction (E) spectra of corresponding films.

### 3.5. Optical Characterization of $ZrO_2@SiO_2$-PDMS

The optical properties of the nanocomposite films were characterized using the lab-built UV-vis spectrometer and the ellipsometer. The transmittance and reflectance spectra of the nanocomposite films were measured using films prepared on coverslips. The air was set to have a transmittance of 100%. The extinction spectra of the film were obtained as described in Equation (1). The transmittance, reflectance, and extinction spectra of 50 wt% $ZrO_2@SiO_2$-PDMS are shown in Figure 5g–i, respectively. Transmittances of the coverslip, PDMS, and $ZrO_2@SiO_2$-18h-PDMS (50 wt%) were, averaged in the wavelength region from 400 to 800 nm, 91.4%, 92.3%, and 91.1%, respectively (Figure 5g). These results were consistent with the digital photographs shown in Figure 5c,f. The reflectance value for the coverslip, PDMS, and $ZrO_2@SiO_2$-18h-PDMS were 7.7%, 7.1%, and 7.6%, respectively (Figure 5h). Extinction spectra were obtained based on the transmittance and reflectance to compare the opaqueness of the nanocomposite films. The extinction values of the coverslip, PDMS, and $ZrO_2@SiO_2$-18h-PDMS were 0.9%, 0.7%, and 1.3%, respectively (Figure 5i). In contrast, 50 wt% $ZrO_2$-PDMS and $ZrO_2@SiO_2$-3h-PDMS exhibited higher extinction than 50 wt% $ZrO_2@SiO_2$-18h-PDMS owing to the large agglomerations of NPs.

Ellipsometry was performed to obtain the refractive index dispersion of the prepared nanocomposite films, as shown in Figure 6 and Figure S3. The refractive index of 50 wt% $ZrO_2$-PDMS could not be obtained because of strong light scattering from the agglomeration of NPs. In the case of 50 wt% $ZrO_2@SiO_2$-3h-PDMS, the refractive index could only be measured in some locations. On the other hand, the refractive indices of both 50 wt% $ZrO_2@SiO_2$-18h-PDMS and $ZrO_2@SiO_2$-54h-PDMS could be measured in every location

because NPs were well-dispersed without any hindrance from light scattering, as shown in Figure 6a. The difference between the refractive indices of $ZrO_2@SiO_2$-18h-PDMS and $ZrO_2@SiO_2$-54h-PDMS was 0.3 at 633 nm, which is consistent with the result shown in Figure 4c. The average transmittances of 50 wt% $ZrO_2@SiO_2$-18h-PDMS and $ZrO_2@SiO_2$-54h-PDMS were 91.1% and 91.3%, respectively; i.e., they had almost the same transmittance (Figure 6a (inset)). The Stöber method with the reaction time of 18 h was selected as optimal for the surface modification of $ZrO_2$ NPs in this work because $ZrO_2@SiO_2$-18h-PDMS had excellent transmittance and high refractive indices.
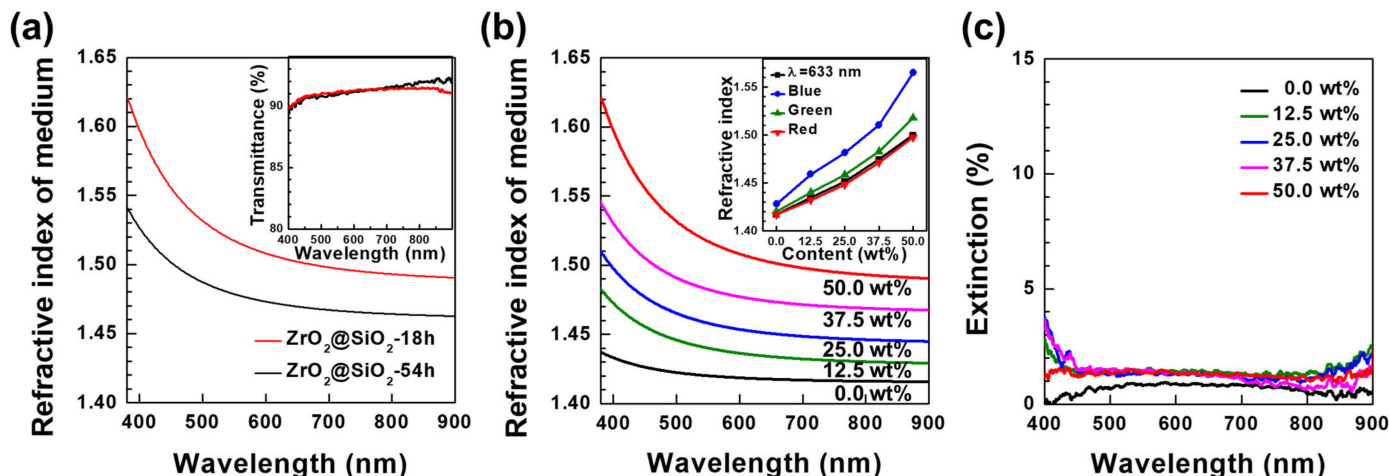


**Figure 6.** (**a**) Refractive index dispersions of (red) $ZrO_2@SiO_2$-18h-PDMS and (black) $ZrO_2@SiO_2$-54h-PDMS nanocomposite films. Films were prepared with particle contents of 50 wt%. The inset shows the transmittance spectra of the corresponding nanocomposite films. (**b**) Refractive index dispersions of $ZrO_2@SiO_2$-18h-PDMS films with different NP contents (0.0 to 50.0 wt%). The inset shows the refractive indices (at (black) $\lambda = 633$ nm and RGB wavelengths selected according to the CIE 1931 color space (blue—$\lambda = 436$ nm, green—$\lambda = 546$ nm, and red—$\lambda = 700$ nm) of the corresponding nanocomposite films. (**c**) Extinction spectra of the corresponding nanocomposite films.

Finally, the refractive index dispersions for $ZrO_2@SiO_2$-18h-PDMS were measured at different NP contents of 0.0, 12.5, 25.0, 37.5, and 50.0 wt%, as shown in Figure 6b. The refractive indices of $ZrO_2@SiO_2$-18h-PDMS with different NP contents were represented at a wavelength of 633 nm and at RGB colors selected according to the CIE 1931 color space; red—$\lambda = 700$ nm, green—$\lambda = 546$ nm, and blue—$\lambda = 436$ nm (Figure 6b (inset), Table S2) [56]. By changing the $ZrO_2@SiO_2$-18h NP content, the refractive index of the $ZrO_2@SiO_2$-18h-PDMS was adjusted from 1.42 to 1.60 in the visible-light region. The light extinction of $ZrO_2@SiO_2$-18h-PDMS was 1.5% or lower, indicating that $ZrO_2@SiO_2$-18h-PDMS achieved excellent transparency with all the studied NP contents (Figure 6c). Scratch resistance is one of the mechanical properties that the developed nanocomposite must obtain in order to be widely used as an advanced optical material. As shown by the scratch test depicted in Figure S5, the $ZrO_2@SiO_2$-18h-PDMS film seemed to have resistance similar to that of a bare PDMS film. It is necessary to improve the surface resistance and mechanical properties of the thin nanocomposite film through follow-up studies on the dispersion of $ZrO_2@SiO_2$ NPs in polymer matrixes that are harder than PDMS, including PET, epoxy, and acrylic resins.

## 4. Conclusions

We demonstrated that $ZrO_2$ NPs could be stably and homogeneously dispersed in PDMS only after surface modification with a thin $SiO_2$ layer using the simple Stöber method. We fabricated $ZrO_2@SiO_2$-PDMS nanocomposite films with adjustable refractive indices and excellent transparency. $ZrO_2$ NPs were synthesized via hydrothermal synthesis, and

their surface modification with a nanometer-thick $SiO_2$ layer was effectively controlled by adjusting the reaction time of the Stöber method. By dispersing surface-modified $ZrO_2@SiO_2$-18h NPs in the PDMS, thin nanocomposite films with high refractive indices and excellent transparency were obtained. The $ZrO_2@SiO_2$-18h-PDMS nanocomposite films exhibited excellent transparency (91.1%), close to that of the coverslip (91.4%) in the visible region, and adjustable refractive indices (1.42–1.60) for the $ZrO_2@SiO_2$ NP content. $ZrO_2@SiO_2$-PDMS nanocomposite films may be useful in developing advanced optical devices based on simple synthesis and fabrication methods.

**Supplementary Materials:** The following supporting information can be downloaded from https://www.mdpi.com/article/10.3390/nano12142328/s1. Figure S1: XRD patterns of $ZrO_2$ NPs; Figure S2: Refractive indices of $ZrO_2$ NP aqueous solutions at $\lambda = 633$ nm with different reaction times; Table S1: Values from the literature for the refractive indices and density of $ZrO_2$, $SiO_2$, and water; Figure S3: Ellipsometric spectra of nanocomposite films; Table S2: Refractive indices of $ZrO_2@SiO_2$-18h-PDMS nanocomposite films prepared with different NP contents; Figure S4: Thicknesses of prepared nanocomposite and PDMS films; Figure S5: The scratch resistance tests for the $ZrO_2@SiO_2$-18h-PDMS nanocomposite film.

**Author Contributions:** Conceptualization, H.C., D.L. and I.Y.; investigation, H.C., D.L., S.H., H.K. and K.J.; writing—original draft preparation, H.C., D.L., C.K. and I.Y.; writing—review and editing, H.C., D.L., C.K. and I.Y.; Methodology, K.J.; supervision, C.K. and I.Y.; funding acquisition, C.K. and I.Y. All authors have read and agreed to the published version of the manuscript.

**Data Availability Statement:** Data presented in this article are available upon request from the corresponding author.

**Conflicts of Interest:** The authors declare no conflict of interest.

# References

1. Loste, J.; Lopez-Cuesta, J.-M.; Billon, L.; Garay, H.; Save, M. Transparent polymer nanocomposites: An overview on their synthesis and advanced properties. *Prog. Polym. Sci.* **2019**, *89*, 133–158. [CrossRef]
2. Pillay, V.; Seedat, A.; Choonara, Y.E.; du Toit, L.C.; Kumar, P.; Ndesendo, V.M.K. A Review of Polymeric Refabrication Techniques to Modify Polymer Properties for Biomedical and Drug Delivery Applications. *AAPS PharmSciTech* **2013**, *14*, 692–711. [CrossRef] [PubMed]
3. Althues, H.; Henle, J.; Kaskel, S. Functional inorganic nanofillers for transparent polymers. *Chem. Soc. Rev.* **2007**, *36*, 1454–1465. [CrossRef] [PubMed]
4. Li, S.; Lin, M.M.; Toprak, M.S.; Kim, D.K.; Muhammed, M. Nanocomposites of polymer and inorganic nanoparticles for optical and magnetic applications. *Nano Rev.* **2010**, *1*, 5214. [CrossRef] [PubMed]
5. Qi, D.; Zhang, K.; Tian, G.; Jiang, B.; Huang, Y. Stretchable Electronics Based on PDMS Substrates. *Adv. Mater.* **2021**, *33*, 2003155. [CrossRef]
6. Haque, S.M.; Ardila-Rey, J.A.; Umar, Y.; Rahman, H.; Mas'ud, A.A.; Muhammad-Sukki, F.; Albarracín, R. Polymeric Materials for Conversion of Electromagnetic Waves from the Sun to Electric Power. *Polymers* **2018**, *10*, 307. [CrossRef]
7. Miranda, I.; Souza, A.; Sousa, P.; Ribeiro, J.; Castanheira, E.M.S.; Lima, R.; Minas, G. Properties and Applications of PDMS for Biomedical Engineering: A Review. *J. Funct. Biomater.* **2022**, *13*, 2. [CrossRef]
8. Zhang, Y.; Zheng, J.; Fang, C.; Li, Z.; Zhao, X.; Li, Y.; Ruan, X.; Dai, Y. Enhancement of silicon-wafer solar cell efficiency with low-cost wrinkle antireflection coating of polydimethylsiloxane. *Sol. Energy Mater. Sol. Cells* **2018**, *181*, 15–20. [CrossRef]
9. Choi, M.-C.; Kim, Y.; Ha, C.-S. Polymers for flexible displays: From material selection to device applications. *Prog. Polym. Sci.* **2008**, *33*, 581–630. [CrossRef]
10. Koshelev, A.; Calafiore, G.; Piña-Hernandez, C.; Allen, F.I.; Dhuey, S.; Sassolini, S.; Wong, E.; Lum, P.; Munechika, K.; Cabrini, S. High refractive index Fresnel lens on a fiber fabricated by nanoimprint lithography for immersion applications. *Opt. Lett.* **2016**, *41*, 3423–3426. [CrossRef]
11. Liu, J.-G.; Ueda, M. High refractive index polymers: Fundamental research and practical applications. *J. Mater. Chem.* **2009**, *19*, 8907–8919. [CrossRef]
12. Jang, J.-Y.; Lee, H.-S.; Cha, S.; Shin, S.-H. Viewing angle enhanced integral imaging display by using a high refractive index medium. *Appl. Opt.* **2011**, *50*, B71–B76. [CrossRef] [PubMed]

13. Novak, B.M. Hybrid Nanocomposite Materials—Between Inorganic Glasses and Organic Polymers. *Adv. Mater.* **1993**, *5*, 422–433. [CrossRef]

14. Van de Hulst, H.C. *Light Scattering by Small Particles*; John Wiley & Sons Inc.: New York, NY, USA, 1957; p. 470. ISBN 978-0486642284.

15. Hajji, P.; David, L.; Gerard, J.F.; Kaddami, H.; Pascault, J.P.; Vigier, G. Synthesis-Morphology-Mechanical Properties Relationships Of Polymer-Silica Nanocomposite Hybrid Materials. *MRS Online Proc. Libr.* **1999**, *576*, 357–362. [CrossRef]

16. Hajji, P.; David, L.; Gerard, J.F.; Pascault, J.P.; Vigier, G. Synthesis, Structure, and Morphology of Polymer–Silica Hybrid Nanocomposites Based on Hydroxyethyl Methacrylate. *J. Polym. Sci. B Polym. Phys.* **1999**, *37*, 3172–3187. [CrossRef]

17. Novak, B.M.; Davies, C. "Inverse" Organic-Inorganic Composite Materials. 2. Free-Radical Routes into nonshrinking sol-gel composites. *Macromolecules* **1991**, *24*, 5481–5483. [CrossRef]

18. Wang, S.; Ahmad, Z.; Mark, J.E. A polyamide-silica composite prepared by the sol-gel process. *Polym. Bull.* **1993**, *31*, 323–330. [CrossRef]

19. Matějka, L.; Dušek, K.; Pleŝtil, J.; Kříž, J.; Lednický, F. Formation and structure of the epoxy-silica hybrids. *Polymer* **1999**, *40*, 171–181. [CrossRef]

20. Wei, Y.; Wang, W.; Yeh, J.-M.; Wang, B.; Yang, D.; Murray, J.K., Jr. Photochemical synthesis of polyacrylate-silica hybrid sol-gel materials catalyzed by photoacids. *Adv. Mater.* **1994**, *6*, 372–374. [CrossRef]

21. Finsel, M.; Hemme, M.; Döring, S.; Rüter, J.S.V.; Dahl, G.T.; Krekeler, T.; Kornowski, A.; Ritter, M.; Weller, H.; Vossmeyer, T. Synthesis and thermal stability of $ZrO_2@SiO_2$ core-shell submicron particles. *RSC Adv.* **2019**, *9*, 26902–26914. [CrossRef]

22. Yang, X.; Zhao, N.; Zhou, Q.; Cai, C.; Zhang, X.; Xu, J. Precise preparation of highly monodisperse $ZrO_2@SiO_2$ core-shell nanoparticles with adjustable refractive indices. *J. Mater. Chem.* **2013**, *1*, 3359–3366. [CrossRef]

23. Zhang, Q.; Shen, J.; Wang, J.; Wu, G.; Chen, L. Sol-gel derived $ZrO_2$-$SiO_2$ highly refractive coatings. *Int. J. Inorg. Chem.* **2000**, *2*, 319–323. [CrossRef]

24. Bai, A.; Song, H.; He, G.; Li, Q.; Yang, C.; Tang, L.; Yu, Y. Facile synthesis of core-shell structured $ZrO_2@SiO_2$ via a modified Stöber method. *Ceram. Int.* **2016**, *42*, 7583–7592. [CrossRef]

25. He, X.; Wang, Z.; Pu, Y.; Wang, D.; Tang, R.; Cui, S.; Wang, J.-X.; Chen, J.-F. High-gravity-assisted scalable synthesis of zirconia nanodispersion for light emitting diodes encapsulation with enhanced light extraction efficiency. *Chem. Eng. Sci.* **2019**, *195*, 1–10. [CrossRef]

26. Tao, P.; Li, Y.; Siegel, R.W.; Schadler, L.S. Transparent dispensible high-refractive index $ZrO_2$/epoxy nanocomposites for LED encapsulation. *J. Appl. Polym. Sci.* **2013**, *130*, 3785–3793. [CrossRef]

27. Cheema, T.A.; Lichtner, A.; Weichert, C.; Böl, M.; Garnweitner, G. Fabrication of transparent polymer-matrix nanocomposites with enhanced mechanical properties from chemically modified $ZrO_2$ nanoparticles. *J. Mater. Sci.* **2012**, *47*, 2665–2674. [CrossRef]

28. Hu, Y.; Gu, G.; Zhou, S.; Wu, L. Preparation and properties of transparent PMMA/$ZrO_2$ nanocomposites using 2-hydroxyethyl methacrylate as a coupling agent. *Polymer* **2011**, *52*, 122–129. [CrossRef]

29. Lee, S.; Shin, H.-J.; Yoon, S.-M.; Yi, D.K.; Choi, J.-Y.; Paik, U. Refractive index engineering of transparent $ZrO_2$-polydimethylsiloxane nanocomposites. *J. Mater. Chem.* **2008**, *18*, 1751–1755. [CrossRef]

30. Guschl, P.; McClintock, G. White Paper: Solvent-Free Formulations with Pixclear® $ZrO_2$ for High-Refractive Index Films. Available online: www.pixelligent.com/white-papers/ (accessed on 10 May 2022).

31. Wehrenberg, B.; Turakhia, D. White Paper: Utilizing Hansen Solubility Parameters for Formulation Optimization Using Pixclear® Zirconia Nanocrystals. Available online: www.pixelligent.com/white-papers/ (accessed on 10 May 2022).

32. Guschl, P.; McClintock, G. White Paper: Solvent-Based Formulations with Pixclear® $ZrO_2$ for High-Refractive Index Films. Available online: www.pixelligent.com/white-papers/ (accessed on 10 May 2022).

33. Gupta, N.S.; Lee, K.-S.; Labouriau, A. Tuning Thermal and Mechanical Properties of Polydimethylsiloxane with Carbon Fibers. *Polymers* **2021**, *13*, 1141. [CrossRef]

34. Arago, D.F.J.; Biot, J.B. Refractive properties of binary mixtures. *Mém. Acad. Fr.* **1806**, 7–9.

35. House, K.A.; House, J.E. Thermodynamics of dissolution of urea in water, alcohols, and their mixtures. *J. Mol. Liq.* **2017**, *242*, 428–432. [CrossRef]

36. Kubo, S.; Diaz, A.; Tang, Y.; Mayer, T.S.; Khoo, I.C.; Mallouk, T.E. Tunability of the Refractive Index of Gold Nanoparticle Dispersions. *Nano Lett.* **2007**, *7*, 3418–3423. [CrossRef]

37. Gates-Rector, S.; Blanton, T. The Powder Diffraction File: A Quality Materials Characterization Database. *Power Diffr.* **2019**, *34*, 352–360. [CrossRef]

38. Bumajdad, A.; Nazeer, A.A.; Sagheer, F.A.; Nahar, S.; Zaki, M.I. Controlled Synthesis of $ZrO_2$ Nanoparticles with Tailored Size, Morphology and Crystal Phases via Organic/Inorganic Hybrid Films. *Sci. Rep.* **2018**, *8*, 3695. [CrossRef] [PubMed]

39. Moulder, J.F.; Stickle, W.F.; Sobol, P.E.; Bomben, K.D. References. In *Handbook of X-ray Photoelectron Spectroscopy*; Chastian, J., King, R.C., Jr., Eds.; Physical Electronics, Inc.: Eden Prairie, MN, USA, 1995; pp. 44, 56, 108. ISBN 0-9648124-1-X.

40. Nalbandian, L.; Patrikiadou, E.; Zaspalis, V.; Patrikidou, A.; Hatzidaki, E.; Papandreou, C.N. Magnetic Nanoparticles in Medical Diagnostic Applications: Synthesis, Characterization and Proteins Conjugation. *Curr. Nanosci.* **2016**, *12*, 455–468. [CrossRef]

41. Zhang, Q.; Zhang, T.; Ge, J.; Yin, Y. Permeable Silica Shell through Surface-Protected Etching. *Nano Lett.* **2008**, *8*, 2867–2871. [CrossRef] [PubMed]

42. Maguire, C.M.; Rösslein, M.; Wick, P.; Prina-Mello, A. Characterisation of particles in solution—A perspective on light scattering and comparative technologies. *Sci. Technol. Adv. Mater.* **2018**, *19*, 732–745. [CrossRef]

43. Tauc, J.; Grigorovici, R.; Vancu, A. Optical Properties and Electronic Structure of Amorphous Germanium. *Phys. Status Solidi B* **1966**, *15*, 627–637. [CrossRef]

44. Liu, Y.C.; Tung, S.K.; Hsieh, J.H. Influence of annealing on optical properties and surface structure of ZnO thin films. *J. Cryst. Growth* **2006**, *287*, 105–111. [CrossRef]

45. Tompkins, H.G.; Hilfiker, J.N. *Spectroscopic Ellipsometry: Practical Application to Thin Film Characterization*; Brundle, C.R., Ed.; Momentum Press: New York, NY, USA, 2016; ISBN 978-1-60650-727-8.

46. Jõgiaas, T.; Kull, M.; Seemen, H.; Ritslaid, P.; Kukli, K.; Tamm, A. Optical and mechanical properties of nanolaminates of zirconium and hafnium oxides grown by atomic layer deposition. *J. Vac. Sci. Technol. A* **2020**, *38*, 022406. [CrossRef]

47. Shukla, S.; Seal, S. Mechanisms of room temperature metastable tetragonal phase stabilization in zirconia. *Int. Mater. Rev.* **2005**, *50*, 45–64. [CrossRef]

48. Dixit, C.K.; Bhakta, S.; Kumar, A.; Suib, S.L.; Rusling, J.F. Fast nucleation for silica nanoparticle synthesis using a sol-gel method. *Nanoscale* **2016**, *8*, 19662–19667. [CrossRef] [PubMed]

49. Hale, G.M.; Querry, M.R. Optical Constants of Water in the 200-nm to 200-μm Wavelength Region. *Appl. Opt.* **1973**, *12*, 555–563. [CrossRef]

50. Rouseel, P.J.; Vanhellemont, J.; Maes, H.E. Numerical aspects of the implementation of effective-medium approximation models in spectroscopic ellipsometry regression software. *Thin Solid Films* **1993**, *234*, 423–427. [CrossRef]

51. Garnett, J.C.M. Colours in metal glasses and in metallic films. *Philos. Trans. R. Soc. A* **1904**, *203*, 385–420. [CrossRef]

52. Garnett, J.C.M. Colours in metal glasses, in metallic films, and in metallic solutions II. *Philos. Trans. R. Soc. A* **1906**, *205*, 237–288. [CrossRef]

53. Zhang, X.; Ye, H.; Xiao, B.; Yan, L.; Lv, H.; Jiang, B. Sol-Gel Preparation of PDMS/Silica Hybrid Antireflective Coatings with Controlled Thickness and Durable Antireflective Performance. *J. Phys. Chem. C* **2010**, *114*, 19979–19983. [CrossRef]

54. Compoint, F.; Fall, D.; Piombini, H.; Belleville, P.; Montouillout, Y.; Duquennoy, M.; Ouaftouh, M.; Jenot, F.; Piwakowski, B.; Sanchez, C. Sol-gel-processed hybrid silica-PDMS layers for the optics of high-power laser flux systems. *J. Mater. Sci.* **2016**, *51*, 5031–5045. [CrossRef]

55. Klonos, P.; Bolbukh, Y.; Koutsiara, C.S.; Zafeiris, K.; Kalogeri, O.D.; Sternik, D.; Derylo-Marczewska, A.; Tertykh, V.; Pissis, P. Morphology and molecular dynamics investigation of low molecular weight PDMS adsorbed onto Stöber, fumed, and sol-gel silica nanoparticles. *Polymer* **2018**, *148*, 1–13. [CrossRef]

56. Guild, J. The colorimetric properties of the spectrum. *Philos. Trans. R. Soc. A* **1931**, *230*, 149–187. [CrossRef]